Dispersion of strongly confined channel plasmon polariton modes

Zenin, Vladimir; Volkov, Valentyn S.; Han, Zhanghua; Bozhevolnyi, Sergey I.; Devaux, Eloïse; Ebbesen, Thomas W.

Published in:
Journal of the Optical Society of America B: Optical Physics

DOI:
10.1364/JOSAB.28.001596

Publication date:
2011

Document version
Submitted manuscript

Dispersion of strongly confined channel plasmon polariton modes

Vladimir A. Zenin,[1,*] Valentyn S. Volkov,[2] Zhanghua Han,[2] Sergey I. Bozhevolnyi,[2] Eloïsa Devaux,[3] and Thomas W. Ebbesen[3]

[1]*Laboratory of Nanooptics and Femtosecond Electronics, Department of General Physics, Moscow Institute of Physics and Technology (State University), 9, Institutsky Lane, Dolgoprudny, 141700, Russia*
[2]*Institute of Technology and Innovation, University of Southern Denmark, Niels Bohrs Allé 1, DK-5230 Odense M, Denmark*
[3]*Laboratoire des Nanostructures, ISIS, Université de Strasbourg, CNRS (UMR7006), 8 allée Gaspard Monge, 67000 Strasbourg, France*
**Corresponding author: vz@iti.sdu.dk*

Received March 16, 2011; accepted April 19, 2011;
posted May 4, 2011 (Doc. ID 144219); published June 3, 2011

We report on experimental (by use of scanning near-field optical microscopy) and theoretical investigations of strongly confined ($\sim\lambda/5$) channel plasmon polariton (CPP) modes propagating at telecom wavelengths (1425–1630 nm) along V-grooves cut in a gold film. The main CPP characteristics (mode index, width, and propagation length) are determined directly from the experimental near-field images and compared to theoretical results obtained using an analytic description of CPP modes supported by (infinitely deep) V-grooves and finite-element simulations implemented in COMSOL. © 2011 Optical Society of America

OCIS codes: 230.7380, 000.2700.

1. INTRODUCTION

Surface plasmon polaritons (SPPs) represent electromagnetic excitations that are bound to metal-dielectric interfaces [1]. Their fundamental properties have been the subject of extensive studies both theoretical and experimental. In recent years, the focus of investigation shifted noticeably toward exploring the possibilities for SPP control and manipulation with artificially created surface structures. The developments in plasmonic circuitry [2] suggest abundant possibilities for further advancement toward practical realization of exciting optical phenomena associated with metal nanostructures. Thus, the phenomenon of nanoscale field confinement by SPP manipulation has great potential to revolutionize many applications in nanophotonics, ranging from quantum optics [3] to imaging [4], near-field optics [5,6], and nanosensing [7].

Note that the physics of SPP guiding is fundamentally different from that of light guiding in dielectric waveguides (which obey the diffraction limit) and is intimately connected with the hybrid nature of SPP modes, in which electromagnetic fields in dielectrics are coupled to free electron oscillations in metals [1]. A variety of SPP guiding geometries have already been suggested to achieve high SPP concentration on length scales smaller than the diffraction limit of light (in the surrounding dielectric) [2]. The appropriate SPP modes are supported, for example, by linear chains of metal nanoparticles [8], narrow dielectric ridges deposited on metal films known as dielectric-loaded SPP waveguides (DLSPPWs) [9], narrow gaps between metal surfaces (gap SPPs) [10], and by corresponding cylindrical, i.e., rod and coaxial, structures [11,12]. Since, for all of these SPP systems (except DLSPPWs), the downscaling of cross section is not limited by the light wavelength, they represent a promising alternative to dielectric optical waveguides. However, the simultaneous realization of strong confinement and a propagation loss sufficiently low for practical applications has long been out of reach.

Channel SPP modes—channel plasmon polaritons (CPPs)—are electromagnetic waves that are bound to and propagate along the bottom of V-shaped grooves milled in a metal film [13]. They are expected to exhibit useful subwavelength confinement, relatively low propagation loss [14], single-mode operation [15], and efficient transmission around sharp bends [16]. Recent experiments showed that CPPs at telecom wavelengths propagate over tens of micrometers along grooves in gold [17] and exhibit strong subwavelength confinement along with low bend losses in large-angle S-bends and Y-splitters [18], thereby enabling the realization of ultracompact plasmonic components such as Mach–Zehnder interferometers, waveguide-ring (WR) resonators [19], add-drop multiplexers, and compact Bragg grating filters [20] as well as nanofocusing components [21]. Thus, there is substantial interest in the fundamental properties of CPP propagation in metal V-grooves, which are determined by the dispersion properties of the CPP mode. Knowledge of CPP modal shape and dispersion properties is essential to set up an efficient end-fire excitation of the waveguide, and also to estimate efficient coupling between adjacent waveguides. In contrast to the dispersion relation for a SPP at a planar metal/dielectric interface, which is well investigated theoretically and experimentally (as well as for different planar waveguide configurations) [1,22,23], the dispersion of CPP modes and their field profiles in V-grooves has to date only been investigated theoretically [13,17,24–28].

In this paper, we report on experimental (by use of scanning near-field optical microscopy) and theoretical

investigations of the dispersion and the mode structure of strongly confined CPP modes propagating at telecommunication wavelengths along V-grooves cut in a gold film.

2. EXPERIMENTAL ARRANGEMENT

The sample, containing several straight 150 μm long V-shaped grooves with the angle θ close to ~17° and depth d of ~1.7 μm, was fabricated using a focused ion-beam (FIB) milling technique in a 2-μm-thick gold layer deposited on a substrate of fused silica covered with an 80-nm-thick indium-tin-oxide layer [Fig. 1(a)]. For these groove parameters, the CPP guiding is expected to be single-mode [17]. Special care was taken to fabricate V-grooves with smooth walls and prevent contamination of the completed structures by dust particles.

The experimental setup is rather similar to that used in our previous experiments [17–21] and consists of a collection scanning near-field optical microscope (SNOM) with an uncoated sharp fiber tip used as a probe and an arrangement for launching tunable (1430–1620 nm) TE/TM-polarized radiation into a metal groove by positioning a tapered-lensed polarization-maintaining single-mode fiber [Fig. 1(b)]. Note that, since the main component of the SPP electric field is oriented perpendicularly to the metal surface [1], the CPP electric field tends to be oriented perpendicularly to the groove walls and thereby, for small groove angles, parallel to the sample surface plane. The adjustment of the in-coupling fiber with respect to the illuminated V-groove channel was accomplished during monitoring of the SPP propagation along the sample surface with the help of a far-field microscopic arrangement. The track of the propagating radiation (distinguishable for all structures and wavelengths) featured, apart from a gradual decay in visibility with the propagation distance, a rather bright spot at its termination [Fig. 1(c)]. These far-field observations also confirmed the expected polarization properties of the guided radiation [17] and demonstrated its (relatively) low dissipation. Following these experiments (that also include adjusting the in-coupling fiber position to maximize the coupling efficiency), we moved the entire fiber-sample arrangement under the SNOM head and mapped the intensity distribution near the surface of the groove with an uncoated sharp fiber tip of the SNOM. The near-field optical probe used in the experiment was produced from a single-mode silica fiber by ~120 min etching of a cleaved fiber in 40% hydrofluoric acid with a protective layer of olive oil. The resulting fiber tip has a cone angle of ~30° and curvature radius of less than 100 nm [Fig. 1(d)].

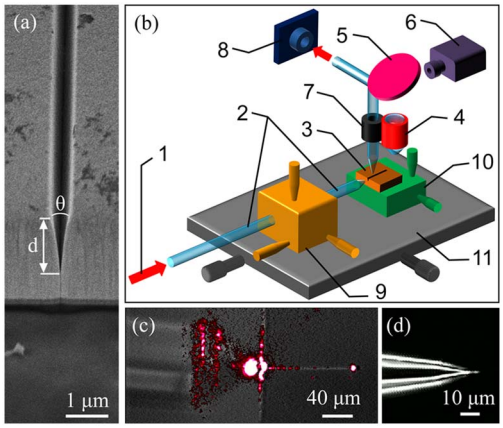

Fig. 1. (Color online) Experimental arrangement. (a) SEM image of V-groove entrance showing typical groove profile (d and θ are groove depth and angle, respectively). (b) Schematic layout of the experimental setup. (1) TE-polarized radiation (electric field is parallel to sample surface plane) from tunable laser (1425–1630 nm); (2) in-coupling tapered-lensed polarization-maintaining single-mode fiber; (3) sample: gold film containing several straight V-grooves; (4) microscope objective of 20× magnification; (5) mirror; (6) IR camera; (7) SNOM operated in collection mode; (8) InGaAs photoreceiver; (9) three-dimensional X, Y, Z stage; (10),(11) two-dimensional X, Y stages. (c) Microscope image of a coupling arrangement superimposed with far-field image taken at excitation wavelength $\lambda \approx 1600$ nm with IR camera, showing the track of CPP propagation and a bright spot at the V-groove termination. (d) Microscope image of near-field optical probe used in the experiment.

The tip was scanned along the sample surface at a constant distance of a few nanometers maintained by shear-force feedback. It should be noted that this distance could not be maintained in the middle of the groove (given the groove dimensions and the tip size), a circumstance that might influence the characterization of CPP mode cross section. Near-field radiation scattered by the tip was partially collected by the fiber itself and propagated in the form of the fiber modes toward the other end of the fiber, where it was detected by a femtowatt InGaAs photoreceiver.

3. EXPERIMENTAL RESULTS

The fabricated plasmonic structures were excited at different wavelengths ranging from 1425 to 1630 nm with TE-polarized light and imaged with SNOM. Topographical and near-field optical images of efficient CPP guiding by fabricated V-grooves were recorded at the distance of ~100 μm from the in-coupling groove edge (to decrease the influence of the stray light., i.e., the light that was not coupled into the CPP mode) and in the entire range of laser tunability.

The experimental results (typical topographical and near-field optical images of CPP propagation at different wavelengths) can be seen in Fig. 2, where the SNOM images are oriented in such a way that the CPPs propagate from left to right (in the horizontal direction). SNOM measurements were carried out by scanning areas of roughly 36.8 μm × 3.5 μm [Figs. 2(a)–2(c)] and 55 μm × 3.5 μm [Figs. 2(d)–2(h)] along the waveguide. The fast scan direction was orthogonal to the V-groove. Appearance of the optical images is similar to those obtained with photonic crystal waveguides [29], featuring efficient mode confinement (in the lateral cross section) at the groove and clearly pronounced decay (along the propagation direction) of the CPP intensity. The aforementioned decay is found to be wavelength dependent, directly demonstrating (Fig. 2) the observed increase in CPP propagation length along with the corresponding increase in wavelength. The averaged cross sections taken along the propagation direction for optical ($\lambda = 1630$ nm) and corresponding topographical images are shown in Fig. 2(i). One can see that the cross section taken along the optical image demonstrates clearly pronounced (and rather unperiodic) intensity variations along the propagation direction. The latter is usually accounted for by the interference between the CPP mode's incident and scattered (by the groove imperfections and/or stray light [17]) field components. However, the preliminary analysis of these cross sections together with spatial spectra taken for different wavelengths has shown that the situation is quite complicated, because the cross sections/spectra exhibit

several features that are independent of the light wavelength and therefore should be related (in our opinion) to the roughness of groove walls and/or the scanning mechanism of the SNOM (including scanning speed, stability of the SNOM feedback, shape of the SNOM tip, etc.). To test this idea, the optical cross sections (taken at different wavelengths) were directly compared to cross sections taken (along the same direction) for the corresponding topographical images. The results obtained [Fig. 2(i)] revealed a good agreement between topographical and optical profiles (where the minima in the optical signal clearly correspond to the maxima in topography). Note that due to its evanescent nature, the CPP signal measured in the middle of a groove is directly related to the ability of the SNOM fiber tip to penetrate the channel (with the depth of penetration being kept as constant as possible). The cross sections of the topographical images (taken along and across the propagation direction) showed that the penetration depth varied significantly (both in time and space), with the SNOM tip actually being below the sample surface by ~200–600 nm, depending on the tip shape, stability of the scanning process, and/or the quality of the fabricated V-groove. Thus the disappearance of the CPP signal in certain areas of the groove along the propagation direction [clearly seen in some images, e.g., Figs. 2(e)–2(h)] has to be directly attributed to varying penetration depth of the SNOM fiber tip inside the V-groove. Note also that the recorded images are characterized by a high contrast ratio (the ratio of useful CPP signal in the groove to the background signal), i.e., CPP signal drops rapidly outside the groove, indicating the presence of a negligibly weak homogeneous background at the level of ~3% compared to the maximum signal (inside the groove). Despite the aforementioned signal variations, we could use the recorded SNOM images to characterize the structure of the CPP mode and its propagation length. It turned out that in the wavelength range of 1425–1630 nm, the CPP propagation length (determined from the corresponding SNOM images) varied significantly, depending on both the coupling arrangement and wavelength used. To treat SNOM images properly, the following method has been used [Fig. 3(a)]: averaged optical signal profiles (taken along the propagation direction) have been directly extrapolated by the corresponding exponential dependences fitted by the least-squares method (where the CPP propagation length has been obtained from corresponding exponent coefficients). The result (that shows the CPP propagation length as a function of light wavelength) is presented in Fig. 3(b), where the

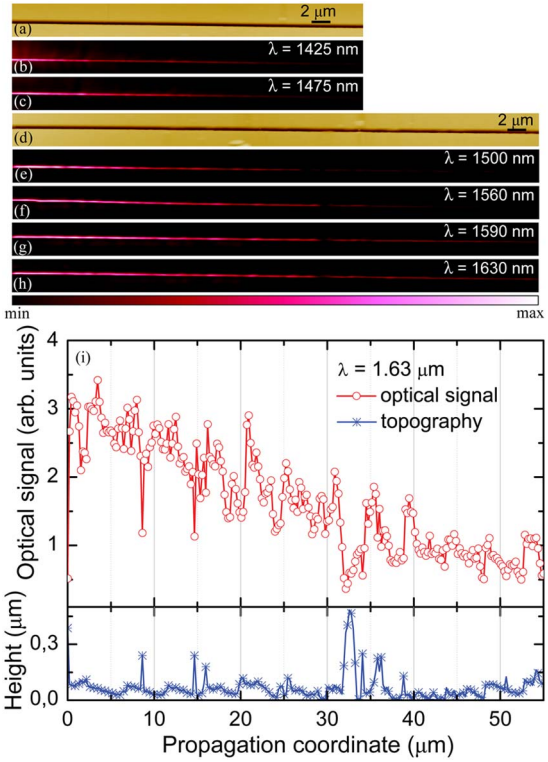

Fig. 2. (Color online) Experimental results. Pseudocolor (a), (d) topographical, and (b)–(c), (e–h) near-field optical images of different sizes; (a–c) 36.8 μm × 3.5 μm, (d–h) 55 μm × 3.5 μm. SNOM images recorded at different wavelengths with shear-force feedback, (b) 1425 nm, (c) 1475 nm, (e) 1500 nm, (f) 1560 nm, (g) 1590 nm, (h) 1630 nm. (i) Cross sections of the topographical (asterisks) and near-field optical (open circles) images of (d), (h) taken (along 1 line) along propagation direction.

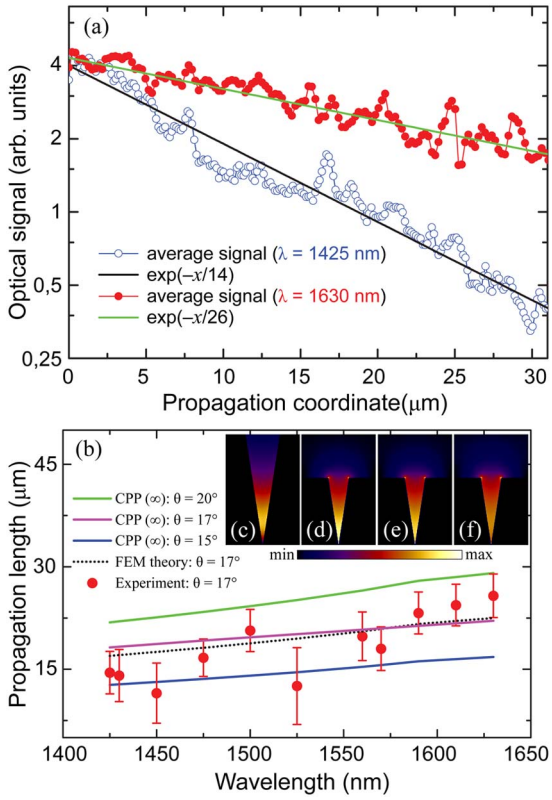

Fig. 3. (Color online) CPP propagation length estimation. (a) Cross sections of the near-field optical images in Figs. 2(b) and 2(h) (filled and open circles, respectively) averaged along 5 lines along the propagation direction; the exponential dependences fitted by the least-squares method to the signal dependence along the propagation direction are included. (b) CPP dispersion: the CPP propagation length as a function of light wavelength; filled circles represent the experimental data, with calculated theoretical curves in different colors. Error bars are estimated from the CPP propagation length maximum variations with the averaging windows at different positions along the propagation direction. Insets (time-averaged electric field distributions) represent the modal structure of the fundamental CPP modes at different wavelengths: (c) CPP (∞) mode for an infinitely deep groove at 1425 nm (computed with EI method); the CPP mode for increasing wavelength of (d) 1425, (e) 1480, and (f) 1630 nm (computed with FEM method for a truncated groove of depth 1.7 μm). Inset size is 2 μm × 3 μm.

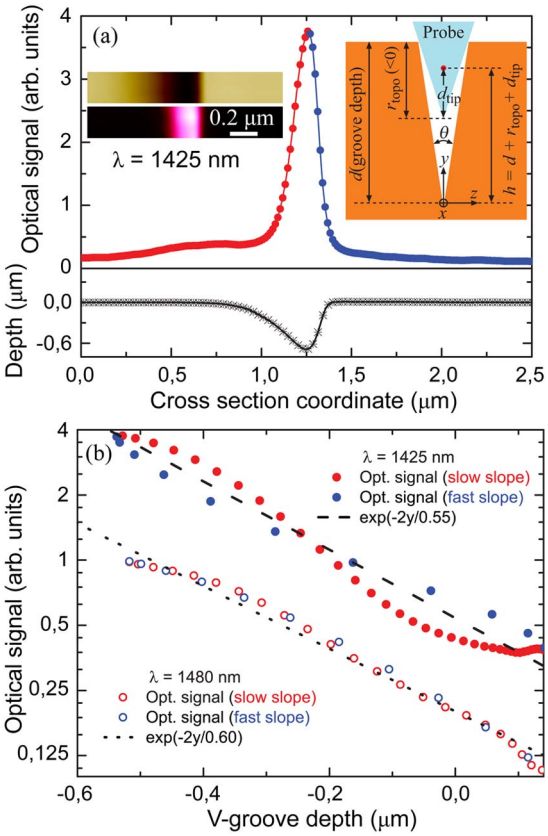

Fig. 4. (Color online) (a) Cross sections of the topographical (asterisks) and corresponding high-resolution near-field optical (filled circles) images (in left-hand insets) averaged along 10 lines perpendicular to the propagation direction. Schematic of the V-groove/SNOM probe configuration under consideration is shown in right-hand inset. (b) Optical signal recorded inside the groove, presented as a function of groove depth, along with the exponential fitting curve.

experimental values (determined through the aforementioned procedure) are shown by the filled circles.

Figure 3(b) also contains results that were calculated theoretically with two different electromagnetic techniques: the first, effective index (EI) approximation [17] in combination with analytic description [28] of CPP modes supported by infinitely deep V-grooves of different angles [shown by solid curves; for simplicity, these modes are labeled as CPP (∞)]; and second, the finite-element method (FEM) as implemented in the commercial software COMSOL (dotted curve), using tabular gold dielectric constants [30]. Overall, it is seen that the experimental results are in rather good agreement (within experimental error) with our calculations, demonstrating a clearly pronounced general trend: the increase in CPP propagation length with the increase in wavelength. Note that the two theoretical approaches provided similar results, as expected for strongly confined (and thereby, far from the cutoff) CPP modes [28]. The same methods have also been used to investigate the structure of the fundamental CPP mode [see insets and legend of Figs. 3(c)–3(f)]. These results show that as the wavelength increased (up to 1630 nm), the field is pushed out of the groove. The latter would facilitate its observation both with a far-field microscope (such a mode is easier to scatter by surface features) and the SNOM (the detection efficiency of a fiber probe increases for lower spatial frequencies [31]). One would expect that (keeping the same trend for even longer wavelengths) there should be a certain cutoff threshold ($\lambda_{\mathrm{cut}} > 1630$ nm) after which the CPP mode can no longer be confined within the groove, and is radiated in the form of SPPs along the contiguous horizontal metal surfaces. It is also observed that as the wavelength increases (i.e., approaching to cutoff), the CPP modes became hybridized with the modes running on the edges at both sides of the groove (e.g., calculations show rather strong hybridization of the CPP mode at $\lambda = 1630$ nm even though it is still mainly confined within the groove walls).

Note that, in our opinion, the roughness and imperfections of V-groove walls (as well as other groove defects) contributed significantly to the detected CPP propagation loss (at least for shorter wavelengths in the range 1425–1525 nm). The discrepancy between theory and experiment can also be ascribed to small differences in the groove geometry, both in the groove shape (e.g., angle, depth, wall flatness) and/or different dielectric permittivities of gold (in our calculations, the Palik and Ghosh [30] data sets were used). For example, it was recently verified [24,27] that even slightly less negative dielectric permittivity of gold or/and smaller groove angle noticeably influences the properties of a CPP mode (including propagation length and cutoff wavelength). One can further suggest that the accuracy of the experimental results can be further improved by increasing the scanning area along the propagation direction of the groove (which should also be combined with a corresponding increase in the number of independent experiments). The latter task is not trivial, considering that the near-field optical microscopy (used in this experiment) is a point-by-point scanning technique (i.e., it is a time-consuming procedure to produce even one SNOM image with a high optical resolution). Despite these difficulties, the high-resolution SNOM images were recorded at different wavelengths (1425 and 1480 nm) and used to investigate the CPP mode characteristics. Figure 4(a) shows typical cross sections (averaged along 10 lines perpendicular to the propagation direction) of high-resolution topographical and corresponding near-field optical images (recorded at $\lambda = 1425$ nm). From the cross sections of the SNOM images, one can see a clearly pronounced asymmetry of topographical and optical profiles (e.g., it is clearly pronounced as a difference in the slope of the groove walls). The latter is not a real topographical/optical artifact (e.g., the actual groove symmetry is revealed by the SEM images in Fig. 1) and should be attributed to a convolution (asymmetry) of the SNOM tip. Generally speaking, every data point in a SNOM image represents a spatial convolution (in the general sense, not in the sense of Fourier analysis) of the shape of the SNOM tip and the shape of the feature imaged (e.g., the V-groove, in

Table 1. Experimental and Numerically Calculated CPP Mode Characteristics

λ	$d_{\mathrm{pen}}(\mathrm{exp})$	$N_{\mathrm{eff}}(\mathrm{exp})$	$w_{\mathrm{FWHM}}(\mathrm{exp})$	$d_{\mathrm{cut}}(\infty)/d_{\mathrm{cut}}(\mathrm{FEM})$	$N_{\mathrm{eff}}(\infty)/N_{\mathrm{eff}}(\mathrm{FEM})$	$w_m(\infty)/w_m(\mathrm{FEM})$
1425 nm	550 nm	1.08	170 nm	650 nm/750 nm	1.064/1.045	288 nm/250 nm
1480 nm	600 nm	1.07	190 nm	679 nm/825 nm	1.059/1.040	310 nm/273 nm

our case). As long as the tip is significantly sharper than the groove the true edge profile of the groove is represented. However, when the feature is sharper than the SNOM tip, the image will be dominated by the tip's shape.

To show experimentally that the power for the CPP mode is indeed efficiently concentrated within the V-groove, one needs to estimate the effective index of the CPP mode. We begin our considerations with the V-groove geometry [see the right-hand inset in Fig. 4(a)] assuming that the groove angle is sufficiently small ($\theta \sim 17°$ as in our experiment). Note that in this case, the SNOM probe can only partially penetrate the groove by a certain depth r_{topo} (which can be evaluated from topographical cross sections of the groove). It is reasonable to assume that the optical signal (collected by the SNOM tip), being proportional to the field intensity (at an effective detection point inside a fiber probe [31]), decreases exponentially with the probe-surface distance [21] (i.e., we are measuring the exponential tail of the CPP field concentrated deep into the groove where it cannot be reached with SNOM probe directly). The latter indicates that the effective index of the CPP mode can be obtained from the decay rate of the CPP field far from the groove bottom, assuming that the decay is exponential with respect to the distance $h = d + r_{\text{topo}} + d_{\text{tip}}$ from the groove bottom ($h > 1\,\mu$m, i.e., we are very close to the V-groove opening). Note that this procedure is essentially approximate because it does not take into account the dependence of the field intensity on the transverse coordinate. For the fiber probe used in our experiments, the effective detection point is found to be located at distance $d_{\text{tip}} \sim 150$ nm away from the fiber tip [31]. The intensity of the field (picked up at the effective detection point of the SNOM tip) as a function of the distance from the groove bottom [Fig. 4(a)] can be presented as follows

$$I(y) \sim \exp(-\alpha h)^2 \approx I_0 \exp(-2r_{\text{topo}}/d_{\text{pen}}), \qquad (1)$$

where $\alpha = 1/d_{\text{pen}} = k_0(N_{\text{eff}}^2 - 1)^{0.5}$ represents the decay rate of the field, $k_0 = 2\pi/\lambda$ is the wave number, λ is the radiation wavelength in vacuum, $N_{\text{eff}} = \beta\lambda/(2\pi)$ is the CPP mode effective index, and β denotes the CPP mode propagation constant. Note that the CPP mode index N_{eff} determines the mode confinement, since the mode penetration depth in dielectric (air) above the sample surface is given by $d_{\text{pen}} = (\lambda/2\pi)\cdot(N_{\text{eff}}^2 - 1)^{-0.5}$, so that a larger effective index corresponds to a smaller penetration depth and thereby better confinement in depth (in width, the CPP mode is confined within the groove walls). To obtain the experimental value of the effective index by measuring the decay rate α, the optical signal has been presented as a function of the groove depth r_{topo} penetrated by the SNOM tip. Thus, the assumption of exponential decay of the CPP field is verified experimentally: Figure 4(b) demonstrates that the intensity of the CPP signal recorded at $\lambda = 1425$ (shown by the filled circles) and 1480 nm (shown by the open circles) indeed decays exponentially with the distance from the groove bottom as $\sim\exp(-2y/0.55)$ for 1425 nm and $\sim\exp(-2y/0.60)$ for 1480 nm. These exponential decays give the CPP mode penetration depth d_{pen} [Eq. (1)] of 550 nm (at $\lambda = 1425$ nm) and 600 nm (at $\lambda = 1480$ nm), and the corresponding experimental $N_{\text{eff}}(\text{exp})$ values are close to 1.08 and 1.07.

This experimental evolution in the CPP field distribution with the groove depth is compared with the fundamental CPP mode profiles calculated with EI (for the infinitely deep groove) and finite-element (for the truncated groove) methods at 1425 and 1480 nm. Here, one should keep in mind that EI method (EIM) usage forces the V-groove CPP fields to approach zero at the groove bottom similarly to the case of CPPs propagating in rectangular grooves (tranches) and for the same reason [27], whereas the CPP field is expected to reach its maximum at the V-groove bottom [13–15]. Influence of the EIM approximation is also reflected in the differences between the effective mode indexes calculated with the FEM, e.g., $N_{\text{eff}}(\text{FEM}) \cong 1.045$, and with EIM $N_{\text{eff}}(\infty) \cong 1.064$ (both found to be smaller than $N_{\text{eff}}(\text{exp})$ estimated experimentally at $\lambda = 1425$ nm). It should be also noted that the y coordinate appearing in Eq. (1) acts as a parameter that determines the V-groove width: $w(y) = 2y\tan(\theta/2)$. To get further theoretical insight into the CPP mode structure, we evaluated the cutoff depth d_{cut} of the V-groove. The latter is the depth (y coordinate) corresponding to the position of the average maximum of the CPP field (i.e., we were looking for $\max[w(y)I_{\text{CPP}}(y)]$); and the groove width at this cutoff depth was considered to be the width of the CPP mode: $w_m = 2d_{\text{cut}}\tan(\theta/2) \approx \theta d_{\text{cut}}$. Thus, for the considered V-groove configuration, the cutoff depths and CPP mode widths calculated (at $\lambda = 1425$ nm) with EIM (for infinitely deep groove), $d_{\text{cut}}(\infty) = 650$ nm and $w_m(\infty) = 288$ nm are found to be quite similar to those obtained with FEM (for finite-depth groove), $d_{\text{cut}}(\text{FEM}) = 750$ nm and $w_m(\text{FEM}) = 250$ nm. In general, it is seen that there is a certain discrepancy between CPP mode characteristics calculated with EIM and FEM. We relate this fact to the circumstance that the correspondence between the EIM (approximate) simulations and accurate numerical modeling (e.g., when using the FEM) is generally worse for channel waveguides [24,26]. Finally, the full width at half-maximum (FWHM) was measured for the experimental mode profiles. The FWHM appeared to be much smaller than the widths calculated numerically (by both EIM and FEM). It can be explained by a strong (nearly exponential) dependence of the CPP field magnitude on the depth coordinate. The deeper the SNOM probe penetrates into the groove, the larger the field magnitude is, so the whole optical profile of the mode becomes narrower. Nevertheless, the measured FWHMs for 1425 and 1480 nm reflect the same trend as for the numerical calculations: the larger the wavelength, the smaller the width.

Summarizing, the CPP mode characteristics determined from high-resolution SNOM images (recorded at 1425 and 1480 nm) through the experimental procedures described here are summarized in Table 1 together with the results of corresponding calculations performed (for the wavelengths and groove parameters used in experiments) by using EIM and FEM.

Note that the calculated effective indexes of the fundamental CPP mode are somewhat smaller than the CPP mode indexes determined from the experimental SNOM images. This discrepancy can be attributed to the aforementioned (small) differences in V-groove shape. One should also keep in mind that the SNOM experiments were conducted at ambient conditions; thus water condensation could not be excluded (a very thin water layer can significantly increase the CPP mode index [24]).

4. CONCLUSION

We have studied the dispersion properties of strongly confined CPP modes propagating at telecom wavelengths (1425–1630 nm) along V-grooves cut in a gold film, inferring the main CPP characteristics (mode index, width, and propagation length) from the experimentally obtained SNOM images and comparing them with simulations results obtained by making use of the analytic description of CPP modes supported by infinitely deep V-grooves [28] and FEM implemented in the commercial software COMSOL. The comparison conducted for CPP propagation length, which was straightforwardly evaluated from the experimental SNOM images, indicated that the difference between the two theoretical approaches is smaller than the uncertainty related to the actual groove profile. Note that for strongly confined (and thereby far from the cutoff) CPP modes, these approaches are expected to provide similar results [28]. It also revealed inherent problems with the experimental SNOM characterization of CPP propagation length related to instabilities in maintaining the same (fiber) tip-surface distance. These instabilities seem to be very difficult to circumvent for sufficiently narrow and deep V-grooves, while those are in fact required to strongly confine CPP modes [24,26–28].

The effective indexes of CPP modes were determined from cross sections of the experimentally obtained topographical and near-field optical images by using exponential fits to the optical signal dependences on the distance between the fiber tip and the groove bottom, a procedure that provides direct access to the mode index while being inherently approximate (as noted in Section 3). Taking this into account, the agreement between the mode indexes determined from the SNOM images and those obtained from the simulations can be considered satisfactory. At the same time, it has to be borne in mind that the former tend to be consistently larger than the latter. Finally, we also found that the evaluation of CPP mode confinement directly from SNOM images can be rather misleading, resulting in underestimation of the mode width (especially for strongly confined CPP modes) because of strong correlation between topological and near-field optical profiles.

Overall, we have fabricated gold V-grooves supporting strongly confined ($\sim\lambda/5$) CPP modes and determined their main characteristics at telecom wavelengths by using the SNOM images. The results obtained are of great importance for further developments in CPP-based plasmonic circuitry [2], where the degree of mode lateral confinement plays a crucial role imposing the upper limit on the density of plasmonic components [27]. In comparison with our first experiments [17–20], the presented CPP waveguides demonstrate an improvement by, at least, 3 times in the lateral mode confinement. Another important conclusion is that the main CPP characteristics can be determined *directly* from the SNOM images, albeit with different levels of accuracy. In this context, our consideration of various issues related to the CPP characterization by using the SNOM provides a firm background for future experimental work, alleviating the need for extensive and time-consuming full-field simulations.

We believe that the results obtained in this work constitute an important step toward developing real-life applications of CPP-based plasmonic circuitry in the fields of optical interconnects and sensing. In this context, a significant challenge yet to be addressed is the realization of efficient in- and outcoupling of radiation, preferably without need for the end-fire coupling with optical fibers that, in fact, can be realized only from one side [17–21]. Strongly confined CPP modes seem especially attractive for sensing applications, in which V-grooves would also be used for microfluidics, since these modes exhibit substantial field enhancements at V-groove bottoms (unlike weakly confined CPP modes [24]). Filling V-grooves with fluids or other materials (e.g., polymers) efficiently represents, however, another formidable challenge that requires further extensive investigations.

ACKNOWLEDGMENTS

The authors gratefully acknowledge financial support from the Danish Council for Independent Research (FTP-project no. 09-072949 ANAP) and the European Research Council (ERC) (grant 227577).

REFERENCES

1. H. Raether, *Surface Plasmons* (Springer, 1988).
2. T. W. Ebbesen, C. Genet, and S. I. Bozhevolnyi, "Surface plasmon circuitry," Phys. Today **61**, 44–50 (2008).
3. D. E. Chang, A. S. Sørensen, E. A. Demler, and M. D. Lukin, "A single-photon transistor using nanoscale surface plasmons," Nature Phys. **3**, 807–812 (2007).
4. N. Fang, H. Lee, C. Sun, and X. Zhang, "Sub-diffraction-limited optical imaging with a silver superlens," Science **308**, 534–547 (2005).
5. N. A. Janunts, K. S. Baghdasaryan, Kh. V. Nerkararyan, and B. Hech, "Excitation and superfocusing of surface plasmon polaritons on a silver-coated optical fiber tip," Opt. Commun. **253**, 118–124 (2005).
6. Y. Wang, W. Srituravanich, C. Sun, and X. Zhang, "Plasmonic near-field scanning probe with high transmission," Nano Lett. **8**, 3041–3045 (2008).
7. M. Ringler, A. Schwemer, M. Wunderlich, A. Nichtl, K. Kurzinger, T. A. Klar, and J. Feldmann, "Shaping emission spectra of fluorescent molecules with single plasmonic nanoresonators," Phys. Rev. Lett. **100**, 203002 (2008).
8. M. Quinten, A. Leitner, J. R. Krenn, and F. R. Aussenegg, "Electromagnetic energy transport via linear chains of silver nanoparticles," Opt. Lett. **23**, 1331–1333 (1998).
9. T. Holmgaard, S. I. Bozhevolnyi, L. Markey, A. Derex, A. V. Krasavin, P. Bolger, and A. V. Zayats, "Efficient excitation of dielectric-loaded surface plasmon-polariton waveguide modes at telecommunication wavelengths," Phys. Rev. B **78**, 165431 (2008).
10. H. Choi, D. F. P. Pile, S. Nam, G. Bartal, and X. Zhang, "Compressing surface plasmons for nano-scale optical focusing," Opt. Express **17**, 7519–7524 (2009).
11. C. A. Pfeiffer, E. N. Economou, and K. L. Ngai, "Surface polaritons in a circularly cylindrical interface: surface plasmons," Phys. Rev. B **10**, 3038–3051 (1974).
12. J. Takahara, S. Yamagishi, H. Taki, A. Morimoto, and T. Kobayashi, "Guiding of a one-dimensional optical beam with nanometer diameter," Opt. Lett. **22**, 475–477 (1997).
13. I. V. Novikov and A. A. Maradudin, "Channel polaritons," Phys. Rev. B **66**, 035403 (2002).
14. D. F. P. Pile and D. K. Gramotnev, "Channel plasmon-polariton in a triangular groove on a metal surface," Opt. Lett. **29**, 1069–1071 (2004).
15. D. K. Gramotnev and D. F. P. Pile, "Single-mode subwavelength waveguide with channel plasmon-polaritons in triangular grooves on a metal surface," Appl. Phys. Lett. **85**, 6323–6325 (2004).
16. D. F. P. Pile and D. K. Gramotnev, "Plasmonic subwavelength waveguides: next to zero losses at sharp bends," Opt. Lett. **30**, 1186–1188 (2005).

17. S. I. Bozhevolnyi, V. S. Volkov, E. Devaux, and T. W. Ebbesen, "Channel plasmon-polariton guiding by subwavelength metal grooves," Phys. Rev. Lett. **95**, 046802 (2005).
18. V. S. Volkov, S. I. Bozhevolnyi, E. Devaux, and T. W. Ebbesen, "Bend loss for channel plasmon polaritons," Appl. Phys. Lett. **89**, 143108 (2006).
19. S. I. Bozhevolnyi, V. S. Volkov, E. Devaux, J.-Y. Laluet, and T. W. Ebbesen, "Channel plasmon subwavelength waveguide components including interferometers and ring resonators," Nature **440**, 508–511 (2006).
20. V. S. Volkov, S. I. Bozhevolnyi, E. Devaux, J.-Y. Laluet, and T. W. Ebbesen, "Wavelength selective nanophotonic components utilizing channel plasmon polaritons," Nano Lett. **7**, 880–884 (2007).
21. V. S. Volkov, S. I. Bozhevolnyi, S. G. Rodrigo, L. Martín-Moreno, F. J. García-Vidal, E. Devaux, and T. W. Ebbesen, "Nanofocusing with channel plasmon polaritons," Nano Lett. **9**, 1278–1282 (2009).
22. G. Schider, J. R. Kren, A. Hohenau, H. Ditlbacher, A. Leitner, F. R. Aussenegg, W. L. Schaich, I. Puscasu, B. Monacelli, and G. Boreman, "Plasmon dispersion relation of Au and Ag nanowires," Phys. Rev. B **68**, 155427 (2003).
23. J. A. Dionne, L. A. Sweatlock, H. A. Atwater, and A. Polman, "Planar metal plasmon waveguides: frequency-dependent dispersion, propagation, localization and loss beyond the free electron model," Phys. Rev. B **72**, 075405 (2005).
24. E. Moreno, F. J. Garcia-Vidal, S. G. Rodrigo, L. Martin-Moreno, and S. I. Bozhevolnyi, "Channel plasmon-polaritons: modal shape, dispersion, and losses," Opt. Lett. **31**, 3447–3449 (2006).
25. I. Lee, J. Jung, J. Park, H. Kim, and B. Lee, "Dispersion characteristics of channel plasmon polariton waveguides with step-trench-type grooves," Opt. Express **15**, 16596–16603 (2007).
26. S. I. Bozhevolnyi and J. Jung, "Scaling for gap plasmon based waveguides," Opt. Express **16**, 2676–2684 (2008).
27. S. I. Bozhevolnyi, "Effective-index modeling of channel plasmon polaritons," Opt. Express **14**, 9467–9476 (2006).
28. S. I. Bozhevolnyi and K. V. Nerkararyan, "Analytic description of channel plasmon polaritons," Opt. Lett. **34**, 2039–2041 (2009).
29. V. S. Volkov, S. I. Bozhevolnyi, L. H. Frandsen, and M. Kristensen, "Direct observation of surface mode excitation and slow light coupling in photonic crystal waveguides," Nano Lett. **7**, 2341–2345 (2007).
30. E. Palik and G. Ghosh, *Handbook of Optical Constants of Solids II* (Academic, 1991).
31. I. P. Radko, I. S. Bozhevolnyi, and N. Gregersen, "Transfer function and near-field detection of evanescent waves," Appl. Opt. **45**, 4054–4061 (2006).